

Models of Direct Time-of-Flight Sensor Precision that Enable Optimal Design and Dynamic Configuration

Lucas J. Koerner, *Member, IEEE*

Abstract—Direct time-of-flight (dToF) sensors that measure depth by pulsing a laser and timing the photon return are used in many applications, including consumer electronics for proximity sensing and depth map generation. A histogram of photon return times is measured and then processed to estimate object depth. By collecting many photons that span multiple bins of the histogram the final depth estimate interpolates between time-to-digital converter bins to produce a result that is more precise than the converter resolution. The precision of this interpolation depends upon the temporal spread of the measurement, the resolution of the time-to-digital converter, and the number of signal and background photons measured. There is a need for dToF depth precision models to guide design and predict and tune performance during use. Here, we present models that estimate sensor depth precision versus dToF design parameters and photons measured. We use Monte Carlo simulations and experimental measurements to prove the accuracy of the models. With proven models in hand, we investigate dToF sensor design by first presenting the dependence of precision upon the TDC resolution and the signal-to-noise ratio. Second, we experimentally measure the depth precision versus the intensity of background illumination. The models closely match the measurements of background susceptibility and locate a transition point of background intensity below which precision is constant and above which the precision continuously degrades. Finally, experimental measurements demonstrate how the modeling enables dynamic tuning: from a single histogram we estimate precision, thus enabling sensor exposure time tuning for a target precision or prediction of the precision given a change in object distance or background illumination. This work presents straightforward models verified by simulation and measurement. These models guide dToF design and enable dynamic adjustments that benefit power-constrained usage scenarios.

Index Terms—ToF, Time-of-Flight, Distance measurement, Single-photon avalanche diode (SPAD), direct time-of-flight (dToF), Histograms, light detection and ranging (LiDAR), Robot sensing systems

I. INTRODUCTION

Optical time-of-flight (ToF) systems consist of a transmitter and a receiver that directly or indirectly time photons to determine the distance to objects. A direct ToF (dToF) sensor probes the scene with a brief laser pulse and measures the time for the reflected photons to return. This approach produces a histogram of photon return times from which the depth and reflectivity of objects in the scene are extracted. Direct ToF examples include a 4,096-pixel sensor that was demonstrated as an altimeter for spacecraft landing [1] and

the miniaturized ST VL53L1X, a 16×16 array with a 4 m range and 1.5 mm precision for mobile phone applications [2]. Direct ToF technology continues to improve suggesting further capability growth. Recent developments include a 3D stacked single-photon avalanche photodiode (SPAD) chip [3], a 256×256 SPAD array chip connected by 3D Cu-Cu stacking to a processing chip [4] and a 1-Mega-pixel time-gated SPAD array (1200×900 SPAD array with $9.4 \mu\text{m}$ pixel pitch) [5].

A single-photon dToF sensor signal chain consists of a pulsed laser diode, an SPAD receiver array, one or more time-to-digital converters (TDCs) that digitize the photon flight time, and memory to build a histogram of the flight times. The pulsed laser, SPAD, and TDC each have an inherent timing jitter, which, when combined with other sources of timing spread that include the distribution of photon travel lengths and weather effects such as fog [6], produce a total temporal spread. Recent work has demonstrated a laser diode driver capable of 64 ps RMS [7]. SPAD miniaturization and integration has progressed with [8] demonstrating an SPAD in 45 nm CMOS image sensor technology with 46 ps RMS timing jitter and no apparent exponential tail due to charge carrier diffusion, such that the timing response is well-modeled by a single Gaussian distribution. Similarly, an SPAD array fabricated in 180 nm CMOS with a $4 \mu\text{m}$ pixel pitch and timing jitter of 88 ps RMS has no apparent exponential tail [9]. A TDC with a resolution of 100 ps and timing jitter of 44 ps RMS was demonstrated previously and is representative of current TDC capabilities [10]. The timing jitter and quantization noise of these three elements may be added in quadrature for a composite RMS uncertainty of ~ 120 ps RMS, equivalent to a distance precision of 18 mm. Yet, considerably more precise measurements are available from both commercial (1.5 mm RMS [2]) and academic devices (1.4 mm RMS [11]). To achieve a depth measurement more precise than the TDC resolution or system temporal spread the TDC histogram is processed using super-resolution localization methods. Here we ask: what analytical models best predict the dependence of the depth precision on instrument timing jitter, TDC resolution, and the number of signal and background photons collected?

Localization of a peak in a histogram or a spot in an image in the presence of noise (Poisson photon and Gaussian instrument) and resolution limits has been studied in several contexts. These contexts include spacecraft star tracking [12], spot localization in fluorescence microscopy (see [13] and reference therein), and processing of LiDAR histograms of photon return times [14]–[16]. Our work draws upon localiza-

L. Koerner is with the Department of Electrical and Computer Engineering, University of St. Thomas, St. Paul MN, 55105 USA e-mail: (koerner.lucas@stthomas.edu).

tion methods from both imaging and LiDAR with analogies between images and timing histograms of: 1) position \Leftrightarrow time; 2) point spread function (PSF) \Leftrightarrow instrument response function (IRF); 3) pixel size \Leftrightarrow histogram bin width. As established by [17] for images, the fundamental precision limit without noise nor pixelization is $\frac{\sigma_{PSF}}{\sqrt{N_{IMG}}}$ where σ_{PSF} is the standard deviation of a Gaussian PSF and N_{IMG} is the number of signal photons measured in the image. The work of Winick [18] establishes the Cramér-Rao bound of the precision of spot localization given a Gaussian PSF, pixelization, and pixel background noise. This previous scenario is analogous to depth estimation from a dToF histogram with the TDC resolution mapping to the image sensor pixelization.

Localization precision has been extensively studied in the field of single-molecule fluorescence microscopy. Similar to dToF depth estimation, spot localization in microscopy estimates the position of a fluorophore in an image captured by an array of pixels that is corrupted by photon shot noise, background photons, pixelization, and image sensor read-noise in 2D [19] or even in 3D dimensions [20]. Spot localization to sub-pixel precision (hence the term super-resolution) has been demonstrated using least-squares (LS) fits [19], maximum-likelihood estimation (MLE) [21], or nonfitting methods such as iterative centroiding of the intensity [22]. MLE approaches the theoretical limit of precision as set by the Cramér-Rao lower bound (CRB) when a model of the microscope PSF and noise is available [13]. This theoretical precision limit has been derived in the presence of photon shot-noise, background photons, and detector pixelization while considering an Airy disk PSF [23].

Return time processing methods for a dToF system may be separated into distinct steps of peak detection and characterization [15]. A dToF system may measure multiple distinct object distances in the scene with more than one and possibly overlapping histogram peaks. In this scenario pre-processing steps such as Richardson-Lucy deconvolution may first be used to minimize the timing spread due to the instrument and recover the resolution of the object [16]. Multiple peaks may be detected using methods such as bump hunting on smoothed derivatives of the photon count data [15] or the reversible jump Markov chain Monte Carlo (RJMCMC) [24]. Once peaks are detected, MLE using a Poisson distribution can be used for the best estimate of the actual return time [15]. These works present optimal processing approaches given specific hardware and/or data as well as innovative approaches to extract multiple peaks in a single histogram. Our goal differs in that we seek to provide models for the localization precision of a single return-time peak. Further, as discussed by Chen et al. [25], LiDAR systems include a number of configurable parameters for which users and designers need guidance. Our models help fulfill this need by guiding the tuning of parameters for optimal performance.

In this work, we present models for the precision of single-photon dToF sensors that link hardware design parameters and the number of signal and background photons collected to the depth precision, thus guiding design and configuration optimization. Our studies present three analytical models of progressively increasing rigor and verify the applicability of

the models using Monte Carlo simulations and experimental measurements. Questions pursued include: 1) How many signal photons are needed for a particular precision? 2) How does precision depend upon the background photon rate? 3) What is the optimal TDC resolution given the temporal spread of the IRF? These models predict the precision from a single histogram and thus support the deployment of adaptive dToF usage including energy-aware algorithms that adjust to the environmental scenario in real-time to enable longer battery life in hand-held applications. Our contribution uniquely presents a straightforward model for timing precision that guides dToF design and configuration.

II. METHODS

A. Analytical modeling

A dToF sensor measures an unknown photon return time, t_0 , in the presence of timing jitter from the laser, SPAD, and TDC. Previous SPAD technologies demonstrated a time response with an exponential diffusion tail following an initial Gaussian response. However, miniaturization and device engineering have eliminated this charge diffusion-based slow exponential tail and justify an assumption of a Gaussian distribution of response times [8], [9], [26]. The temporal spread may be further broadened by details of photon propagation such as measurement of a range of photon path lengths due to object size and the field-of-view of the sensor [27], [28] and atmospheric effects (including fog [6]). We model the combined effects from the sensor and optical propagation as a Gaussian spread of return times with a standard deviation σ . The timing spread of σ may be estimated from a fit to the histogram of return times and used in subsequent modeling as shown in our experimental validation. The models consider the number of signal photons collected to be Poisson distributed with mean value N . This parameter depends upon object reflectivity and depth (d), laser intensity, and sensor exposure time. The timing digitization resolution of the TDC is represented as a . The Poisson distributed background counts per TDC bin is denoted as b . This parameter depends upon the ambient illumination in the environment, the sensor optical and detector design, and the SPAD dark count rate. For a given measurement scenario, with a background photon rate set by the ambient illumination intensity and ToF receiver parameters, b scales with TDC resolution. This scaling makes our analysis distinct from other analyses of microscopy localization where pixel noise may be dominated by electronics noise (i.e. read-noise) and does not scale with pixel size. We note that modeling of optical propagation in a LiDAR system is beyond the scope of this work (for examples see [27], [28]); in this work we experimentally extract these parameters from the sensor histogram to estimate depth precision.

With these parameters in place an expression for the probability distribution function (PDF) of the continuous-time signal is given as:

$$f(t, t_0) = \frac{1}{\sigma\sqrt{2\pi}} e^{-(t-t_0)^2/2\sigma^2}. \quad (1)$$

The signal and background accumulated into a TDC bin that spans a time interval of t_1 to t_2 with $a = t_2 - t_1$ is then given as:

$$Q(t_1, t_2) = \int_{t_1}^{t_2} \frac{N}{\sigma\sqrt{2\pi}} e^{-(t-t_0)^2/2\sigma^2} dt + b. \quad (2)$$

Often instruments have a limit of one photon arrival time digitized per laser pulse, such that the histogram signal is built from many laser pulses.

The dToF localization performance is analytically modeled using three methods. For the case of a Gaussian distributed instrument response function a centroid calculation has been shown to be an unbiased MLE with a one standard deviation uncertainty of:

$$\delta = \sigma/\sqrt{N} \quad (3)$$

when TDC resolution and background noise are ignored [29]. This model is referred to as the fundamental limit. A second localization method presented by Thompson et al. minimizes the least-squares error of a centroid calculation to data that has had a Gaussian mask applied [19]. This method localizes a discretely sampled one-dimensional Gaussian distribution with a precision of:

$$\delta = \sqrt{\frac{\sigma^2 + a^2/12}{N} + \frac{4\sqrt{\pi}\sigma^3 b}{aN^2}}. \quad (4)$$

The third analytical model evaluates the Cramér-Rao bound (CRB) which is the lowest possible variance of an unbiased estimator of an unknown value [30]. The CRB for 1D localization given the PDF of (1) in the presence of quantization, and background noise [18] is:

$$\vec{E}[(t_0(\vec{Q}) - t_0)^2] = \frac{1}{\sum_i \frac{[N f'_i(t_0)]^2}{N f_i(t_0) + b}} \quad (5)$$

where i is the i th TDC bin, f'_i is the derivative with respect to time of the PDF from (1), \vec{Q} represents the measured count values in each TDC bin, and \vec{E} represents the expected value. The actual return time may fall anywhere within the TDC bins and, as such, the estimated variance must be averaged over a full TDC bin of width a to produce a precision estimate of:

$$\delta = \left[\frac{1}{a} \int_{-a/2}^{a/2} \vec{E}[(t_0(\vec{Q}) - t_0)^2] dt_0 \right]^{1/2} \quad (6)$$

This analytical method is referred to as the Cramér-Rao bound (or CRB). We have implemented the CRB calculation in Python and verified concordance with the results in [18].

B. Monte Carlo simulations

We verified the analytical models using Monte Carlo simulations. The Monte Carlo simulation develops an array of Poisson distributed background photon arrival times given a specified average rate that corresponds to b photons per bin. The number of signal photons is determined by drawing from a Poisson distribution with a mean value of N . The arrival time of each signal photon is determined by sampling from a Gaussian distribution with an average arrival time t_0 and a standard deviation set by the temporal spread (σ). With the continuous-time data available, the photon arrival times

are then quantized into bins to emulate the digitization of a TDC. Throughout the simulations, the average arrival time is randomly varied by the width of a histogram bin to remove systematic quantization effects. Fifty histograms are generated for each set of configurations. Note that photon pileup caused by an instrument limit on the number of detected photons per laser pulse, typically one photon per pulse, is not considered in these simulations. Fig. 1 demonstrates a zoom-in around the signal peak of a Monte Carlo simulation result for the scenario of $b = 30.0$, a TDC resolution $a = 150$ ps, and a total of $N = 300$ signal photons.

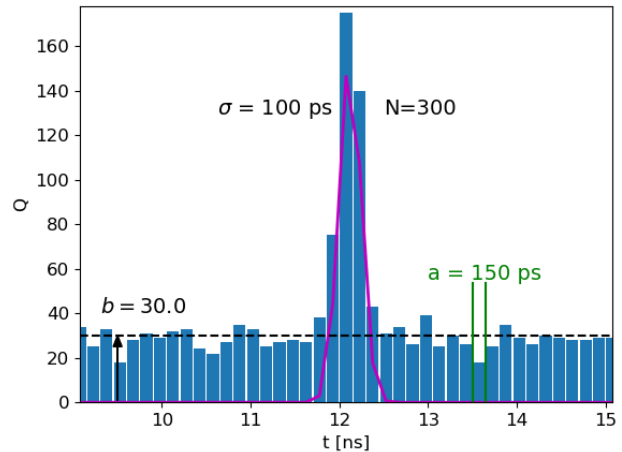


Fig. 1. An example histogram created using Monte Carlo simulations with 176 TDC bins, a background level of $b = 30.0$, total signal photons of $N = 300$, a temporal spread of $\sigma = 150$ ps, and a mean signal arrival time of 12 ns. A Gaussian fit to the histogram data is overlaid in magenta. The plot is zoomed onto a subset of the TDC bins centered around the arrival time of 12 ns.

The generated histograms are localized using multiple approaches. First, the peak is located by finding the mode of the histogram (alternative initial peak finding methods are more capable, e.g. [16], and may locate a peak buried in the noise). Next, the peak is more accurately localized by the following methods:

- 1) A center of mass (CoM) calculation spanning $\pm 3\sigma$ bins from the mode. For a Gaussian distributed instrument response a CoM calculation is a minimum variance estimator.
- 2) A non-linear Gaussian fit to the background-subtracted signal with initial guesses from the known temporal spread (σ) and the amplitude (N) as determined from the mode. The background level is calculated as an average of a set of TDC bins away from the peak.
- 3) A center of mass (CoM) calculation after processing with a Gaussian mask (of standard deviation σ) that is iteratively positioned to follow the best estimate of the peak position as per Thompson [19].

From the peak fits the standard deviation of the difference of the estimated arrival time and the actual arrival time is calculated to be the localization precision (δ). The computer code to run Monte Carlo simulations, evaluate the analytical

models, and create the figures in this manuscript is available on GitHub [31].

C. Experimental verification

We captured experimental measurements with the ST VL53L1X dToF sensor [2], [10] to verify the analytical models and Monte Carlo simulations. The ST VL53L1X is a dToF sensor with a 16×16 array of SPAD pixels and TDCs that create a timing histogram of photon arrivals. The sensor system uses a 940 nm Class 1 pulsed vertical cavity surface emitting laser (VCSEL) that fills the field-of-view (FoV) of the dToF sensor. The FoV is programmable from 15° to 27° . The VL53L1X implements signal processing on the sensor to extract object depth, yet in this work we download the photon arrival histogram and implement peak localization using a Gaussian fit as described in Section II-B. The dToF sensor was tripod mounted with a flat target of uniform reflectivity that filled the field-of-view as in [32]. For controlled background illumination a set of IR light-emitting diodes (LEDs) with a center wavelength of 940 nm and full-width at half-maximum of 80 nm (LST1-01F09-IR04-00) was driven by a programmable DC supply automated using instrument control software [33]. The sensor output data includes a histogram of photon return times. Precision was analyzed using a Gaussian fit to the histogram after first locating the mode. The fit extracts the arrival time and the temporal spread (σ) while the average background counts per TDC bin (b) were determined from reference TDC bins that record immediately before the laser pulses. The precision was calculated from the standard deviation of the peak position of the Gaussian fit to 98 nominally identical measurements.

III. RESULTS

Fig. 2 compares the three analytical calculations of depth precision to the results from Monte Carlo simulations processed with the three different methods as the number of signal photons is varied. The temporal spread is $\sigma = 100$ ps and the TDC resolution is $a = 1.5\sigma$ with a background rate per TDC bin of $b = 18.75$. The fundamental limit ignores TDC quantization and background noise and estimates the smallest precision noise. The CRB consistently estimates a slightly greater error than that of Thompson with the deviation greatest at low signal levels (see Fig. 4). The Monte Carlo results closely track the CRB calculation and provide confidence in the implementation of this model. For the Monte Carlo localization, the precision of the Gaussian fit peak processing method outperforms the CoM and the mask CoM. The CoM calculation does not filter the tails of the IRF and so degrades in low signal-to-noise (SNR) scenarios, whereas the mask CoM performs better in these scenarios since the bins in the tails are deemphasized. The mask CoM however degrades at higher signal levels, which in our case is primarily due to an insufficient number of iterations and target error in the iterative routine. Based on the close correspondence with the Monte Carlo results the CRB analytical approach is deemed the most accurate while the analytical model of Thompson is useful for estimates that provide design intuition. For the remainder of

the manuscript, histograms from Monte Carlo simulations and experimental measurements are localized using a Gaussian fit as this method shows the best precision over a range of SNRs. Note that our goal is not to evaluate the best peak localization method(s), but rather to determine the dependence of localization precision upon instrument and experiment parameters.

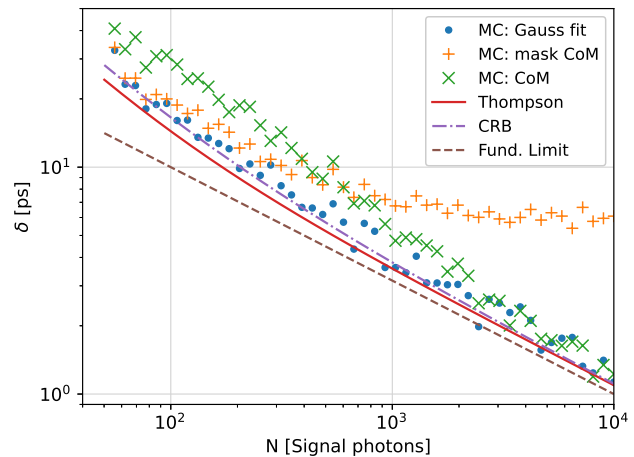


Fig. 2. Lines are analytical calculations of depth precision as the number of signal photons is varied. Markers are results from Monte Carlo (MC) simulations processed with the three different methods to localize the histogram peak. The temporal spread is $\sigma = 100$ ps and the TDC resolution is $a = 1.5\sigma$ with a background per TDC bin of $b = 18.75$.

Fig. 3 assesses the accuracy of the second and third analytical models as compared to Monte Carlo simulations as the number of background photons per bin increases with a constant signal level of $N = 1000$. Again, the CRB more closely tracks the results from the Monte Carlo simulation. Two regimes are evident. At $b < 10$ the background contribution is insignificant such that the precision is dominated by the temporal spread, TDC resolution, and the number of signal photons captured and, as given by (4), plateaus to around $\sqrt{\frac{(100 \text{ ps})^2 + (150 \text{ ps})^2}{1000}} = 3.4$ ps. At high background levels, the precision noise increases as the square-root of the number of background photons as predicted by the second term of (4). Section IV-A further verifies these results with experimental measurements.

The CRB model most closely tracks the Monte Carlo results, particularly when the Monte Carlo simulations are localized using a Gaussian fit to the histogram data. The Thompson model underestimates the precision error because the background noise contribution assumes an infinitesimally small TDC bin size [19]. The deviation of the Thompson model from the CRB and simulations is most significant at high background levels and large TDC bins. Using N/b as the SNR, Fig. 4 displays the percent difference between the CRB model and the Thompson model for N/b from 0.5 to 100 and a/σ from 0.25 to 4. For $a/\sigma \leq 1.2$ the Thompson model deviates from the CRB model but at most by 11%. The most significant deviations are found at low SNR with large TDC bins. The CRB model most accurately tracks the Monte Carlo simulations yet the Thompson model beneficially

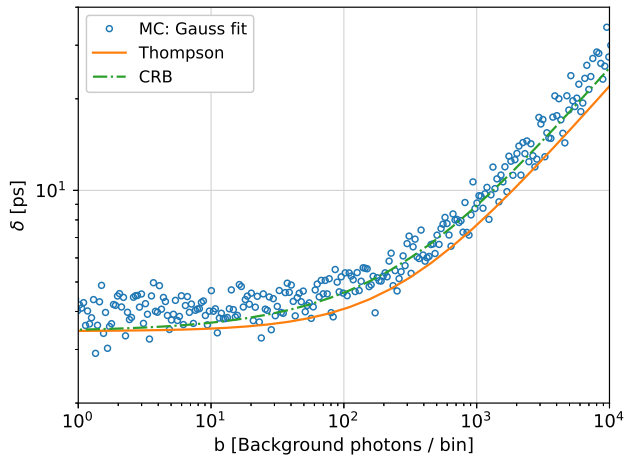


Fig. 3. Lines show analytical calculations while markers show Monte Carlo (MC) results of the depth precision as the number of background photons per bin (b) is varied with a signal level of $N = 1000$ and the same instrument configurations as Fig. 2.

provides a straightforward precision estimate with accuracy within $\approx 20\%$ of the CRB model except for scenarios with both low SNR (< 10) and large TDC bins ($a/\sigma > 2$).

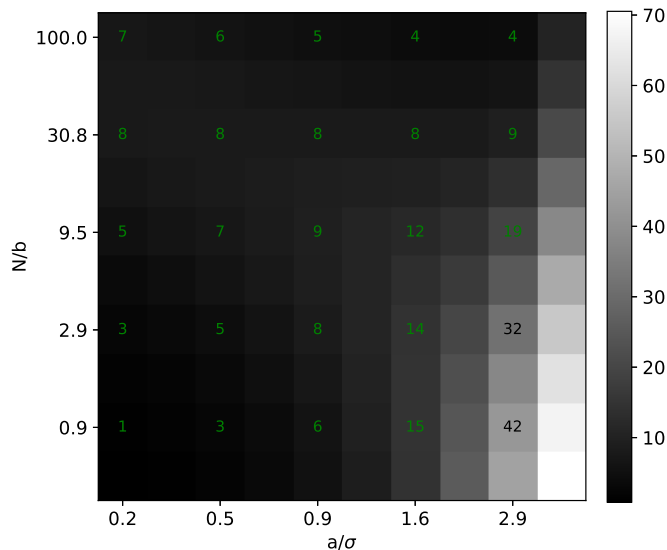


Fig. 4. The percent difference between the CRB timing precision and the Thompson model as the SNR (N/b) and a/σ is varied. In all cases, the CRB precision estimate is greater than the Thompson model.

With confidence in the CRB model and the Monte Carlo simulations, we investigate the optimal TDC resolution for a given temporal spread. Previous work for imaging arrays [18] shows an optimal value of a to be $a \approx 1.5\sigma$ for the case of one-dimensional localization. However, in these scenarios, the background noise is assumed constant independent of pixel

size. For the case of a dToF sensor, in a given environmental scenario with a certain level of ambient illumination, the background rate (r) is constant so that the background counts per TDC bin (b) scales with TDC bin width ($b = ra$). Fig. 5 presents the localization noise as a/σ is varied for four levels of SNR (N/b). Solid lines show the CRB calculation while markers represent the results from the Monte Carlo simulations.

Fig. 5 shows that the smallest precision noise for a given SNR (δ_0 in Table I) is found at $a/\sigma = 0$ which impractically requires a zero width TDC bin. To determine a realistic TDC resolution we set an allowable precision degradation due to finite TDC resolution. To do so, the CRB model is searched for an a/σ value that produces a 10% and 41% increase in precision noise at a particular SNR. The results summarized in Table I suggest an optimum around $a = 1.5\sigma$ if a precision degradation due to TDC resolution of $\leq 10\%$ is targeted. A higher resolution TDC ($a < 1.5\sigma$) does not limit depth precision but is overdesigned and may cost area or power. The CRB projects a continuously growing precision degradation as the TDC bin width becomes much greater than the temporal spread. However, as is shown by the Monte Carlo results of Fig. 5, the precision plateaus at the quantization noise limit (dashed line). In this scenario all the signal photons are confined to a single TDC bin so that interpolation between bins is not possible, thus the precision noise is set only by the resolution of the TDC.

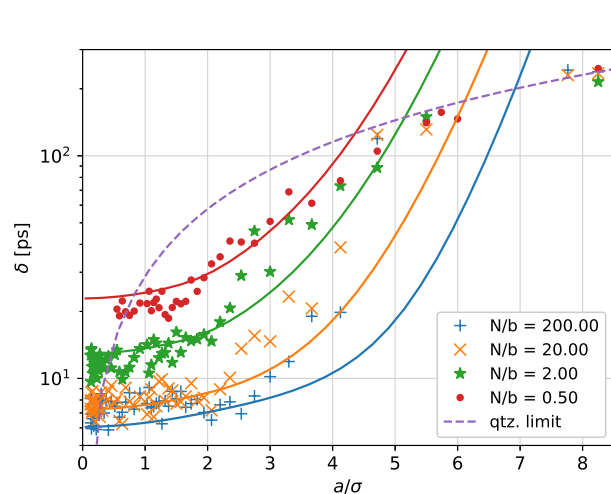


Fig. 5. Monte Carlo simulations as the TDC resolution (a) is swept with a constant temporal spread ($\sigma = 100$ ps). The ratio of total signal photons to background photons per bin (N/b) is indicated in the legend for $a/\sigma = 1$. The background signal per bin is scaled by TDC bin size. The solid lines are the CRB for each of the four N/b levels. The dashed line indicates the limit as set by TDC resolution ($= a/\sqrt{12}$).

IV. CASE STUDIES

Here we leverage the established models to provide guidance relevant to potential dToF design decisions and experimentally demonstrate dynamic tuning of sensor parameters to reach a target precision.

N/b ($a/\sigma = 1$)	a/σ at $\delta = 1.1\delta_0$	a/σ at $\delta = 1.41\delta_0$
200	1.55	3.22
20	1.47	2.78
2	1.35	2.38
0.5	1.31	2.26

TABLE I

TDC BIN RESOLUTION (a) IN TERMS OF THE TEMPORAL SPREAD (σ) THAT PRODUCE A GIVEN PRECISION DEGRADATION FOR VARIOUS LEVELS OF SNR (N/b). THE PRECISION AT $a = 0$ IS REPRESENTED AS δ_0 (NO DEGRADATION). THE SECOND COLUMN SHOWS THE a/σ VALUES FOR A 10% DEGRADATION OF PRECISION FROM THE ZERO TDC BIN WIDTH BASELINE, WHILE THE THIRD COLUMN SHOWS THE SAME FOR A 41% DEGRADATION.

A. Ambient susceptibility

At what level of ambient intensity does the precision of a dToF sensor degrade and how does this ambient susceptibility depend upon design parameters? Fig. 6 shows experimental measurements of the timing precision at an object distance of 1.5 m overlaid with the CRB model versus background photons per bin. The measurement is repeated for four exposure times at varying levels of interfering IR LED intensity. Gaussian fits to the histogram data determined $\sigma = 745$ ps and a TDC resolution of $a = 1067$ ps. For each exposure time, the CRB model uses a constant N , σ , and a as determined from a dataset measured with the interfering IR LEDs off while the background signal (b) is determined from the experimental data. The measured data covers an SNR range of 97.8 to 0.38 through which the CRB model tracks the experimental measurements accurately. At the shortest exposure time of 5 ms the method to localize the histogram peak fails at the highest levels of background photons.

The Thompson noise expression provides intuition to determine the level of background beyond which the depth precision is degraded. By equating the left-term (temporal spread, TDC resolution) of (4) to the right-term (background noise) we find an expression for the number of background photons needed to increase the timing noise by $\sqrt{2}$ from the zero background baseline. This number of background photons per bin or equivalently the product of background rate (r), TDC resolution, and the number of laser pulses (P) is found to be:

$$b = raP = \frac{(\sigma^2 + a^2/12)aN}{4\sqrt{\pi}\sigma^3}. \quad (7)$$

These values are shown as stars in Fig. 6 and lie 13% below the CRB curve since the Thompson estimation underestimates the contribution from background photons to the precision noise. When the temporal spread dominates quantization noise ($\sigma^2 \gg a^2/12$) the background rate (r) that increases the noise by $\sqrt{2}$ follows the number of signal photons received per pulse and is inversely proportional to the temporal spread: $r = \frac{N/P}{4\sqrt{\pi}\sigma}$. The ambient rejection of a dToF sensor (often reported in lux) is improved by a decrease in the temporal spread and an increase in laser power or detector collection efficiency.

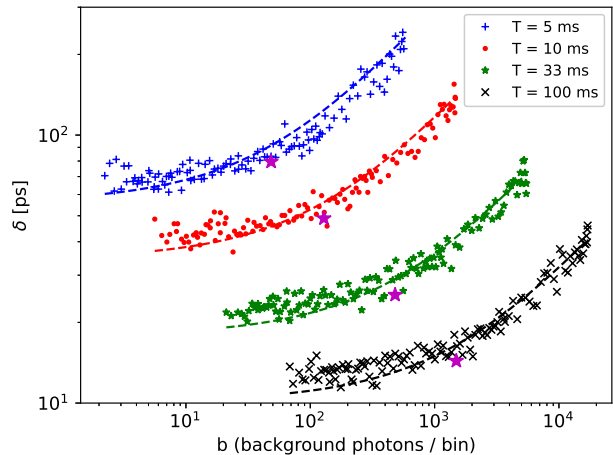


Fig. 6. Experimental measurements of precision versus background photons for exposure times of $T = 5, 10, 33,$ and 100 ms. For each exposure time, the CRB model is indicated as a dashed line. Experimental measurements extracted $\sigma = 745$ ps and a TDC resolution of $a = 1067$ ps. The point where precision is degraded by $\sqrt{2}$ of the zero background baseline is indicated by a $*$ as calculated by (4).

B. Tuning laser intensity and exposure time

How should laser power and exposure time be adjusted for a given target precision? Both the signal and background photon terms in (4) can be written as the product of a rate of arrival and the number of laser pulses (P). To clarify the sources of precision noise we use $N = sP$ where s is the signal returned per pulse and $b = raP$ where r is the background rate in photons/s and find:

$$\delta \propto \sqrt{\left[\underbrace{\sigma^2}_{\text{spread}} + \underbrace{\frac{a^2}{12}}_{\text{resolution}} + \underbrace{\frac{4\sqrt{\pi}\sigma^3}{a} \left(\frac{ra}{s}\right)}_{\text{background}} \right] \frac{1}{sP}} \quad (8)$$

which shows that the precision noise decreases with the inverse of the square root of the number of laser pulses. The ratio of $\frac{ra}{s}$ is the inverse of the SNR: $SNR = \frac{s}{ra} = \frac{N}{b}$ which depends upon the laser intensity, the object distance and reflectivity, and the ambient illumination. The first two terms in brackets are independent of the SNR, while the impact of the third term upon precision is reduced as the SNR increases. At a ratio of total signal photons to background photons per bin of

$$\frac{N}{b} = \frac{48\sqrt{\pi}\sigma^3}{12\sigma^2 a + a^3} \quad (9)$$

the background contribution to the noise is equal to the contributions from the temporal spread and the TDC resolution. This value of N/b is 2.66 when the TDC resolution is given as $a = 2\sigma$. Fig. 7 shows this transition point as a $*$ and demonstrates two regimes of the precision noise. At low N the noise is dominated by the background and scales as $1/N$ while at high N the noise is limited by the signal and scales as $1/\sqrt{N}$. Since the power consumption of the laser is the product of the number of pulses (P) and the laser photons per pulse (s) an increase in laser power and an increase in

laser pulses (i.e. exposure time) impact the power consumption equally. For power-efficient operation with the best possible precision, the laser intensity should be increased so that the background term in (8) contributes minimally. Once this signal rate is reached a reduction in precision noise is accomplished nearly equally by an increase in laser intensity, $\delta \propto 1/\sqrt{s}$, or by an increase in exposure time, $\delta \propto 1/\sqrt{P}$. The proper parameter to adjust can then be determined by constraints such as motion blurring, laser capabilities, or eye safety.

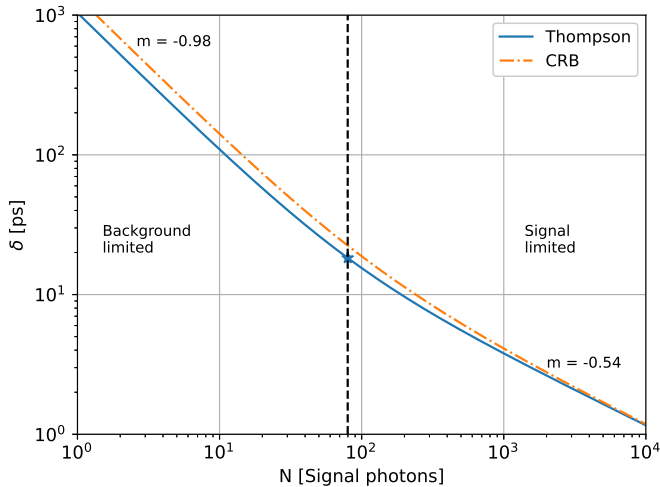


Fig. 7. A demonstration of the two SNR regimes. The number of signal photons are varied while the background photons are held constant ($b = 30$) with $\sigma = 100$ ps and $a = 2\sigma$. The precision noise is shown as calculated by the Thompson expression (4) and the CRB (6). The two regimes are separated by a dashed line with the background limited regime to the left and the signal photon limited regime to the right. The slopes of linear fits to $\log(N)$ vs. $\log(\delta)$ of the CRB estimate are annotated as $m = -0.98$ and $m = -0.54$.

C. Experimental demonstration of dynamic precision tuning

The CRB precision model can be used to tune sensor configuration and predict performance. From a single histogram the signal, background, and temporal spread can be extracted and used as inputs to the model. Table II demonstrates this possibility using experimental measurements captured with the VL53L1X dToF sensor. Each row of the table represents a specific set of distance (d), exposure time (T), and intensity of interfering IR background. For the configuration of each row, 98 measurements were captured with the estimated precision calculated from single histograms using the CRB model (Est. δ) and the measured precision evaluated as the standard deviation of the histogram localization using a Gaussian fit (Meas. δ). For each of the three cases in the table we demonstrate how the CRB precision estimate from a probe measurement can be used to dynamically tune the dToF sensor configuration or predict performance after an environmental change.

Consider case 1 in Table II with an object depth of 800 mm and an exposure time of $T = 33$ ms. A hypothetical power-aware use case (dynamic A) that requires only 0.5% precision could be tuned to a shorter exposure time. A single-shot probe measurement captured at $T = 33$ ms was used to determine this updated exposure time by an exhaustive search of the CRB

model with the signal and background photons scaled by a ratio of the two exposure times. This search finds that closest available exposure time of $T = 10$ ms. At this exposure time the model predicted a precision of $\delta = 3.80$ mm and we measured a precision of 4.89 mm. In this example, the adjustment to the exposure time reduces the laser power by a factor of $\times 3.3$, thus saving power. Similarly, a second hypothetical scenario may require more precision ($\delta = 1.0$ mm) than predicted by the probe measurement and thus the exposure time is tuned to 150 ms (see case 1, dynamic B). Case 2 extends this dynamic approach to a scenario with the object distance changing from d to d' thus scaling the signal photons received by a factor of $(d/d')^2$. The signal and background values measured at the probe position allow for predictions of N and b values at the new object distance. We input these values to the CRB model and predict the updated precision (case 2, dynamic A) or determine the required exposure time to maintain the precision (case 2, dynamic B). The example of case 3 uses the CRB model to predict precision performance at a longer range with minimal background given a measurement with considerable background at a closer range. Here, the prediction at the updated distance scales the signal photons by $(d/d')^2$ and assumes the background signal to be that measured with no interfering IR intensity. The dynamic A entry of case 3 shows predicted and measured precisions of 4.71 mm and 4.84 mm, respectively. Table II illustrates how the CRB noise modeling allows measurements from a single histogram measurement to predict precision given configuration adjustments or changes in the environment such as object distance or background intensity.

V. DISCUSSION AND CONCLUSION

Experimental evaluation of dToF sensors often report depth precision and allowable ambient intensity, yet models that predict these results from design parameters and the measured signal and background are not readily available. The straightforward expression of (4) for depth precision allows for dToF design and usage insight and correctly predicts transition points between signal limited and background limited precision. However, this model underestimates the localization noise because the derivation of the background noise term considers the pixel size to be infinitesimal. The CRB model of (6) integrates the background noise over the pixel size and thus, tracks the Monte Carlo simulation results more closely than the Thompson model. As shown in Figures 2, 3, and 5, Monte Carlo simulations with the histogram location extracted by a Gaussian fit accurately track the CRB precision estimate versus signal photons, background photons, and TDC resolution, respectively. The models recommend a TDC resolution of $a \approx 1.5\sigma$, determine the background signal beyond which precision degrades, and show that an increase in laser intensity is more impactful than an equivalent increase in exposure time when the precision is background limited.

In addition to design intuition, models that predict precision enable efficient usage of dToF sensors. From a single return time histogram the depth precision can be estimated to enable sensor configuration adjustments that target a specific

Case	Description	d [mm]	T [ms]	N	b	σ/a	Est. δ [mm]	Meas. δ [mm]	Pred. δ [mm]
1	probe	800	33	7224	517	0.807	2.11 \pm 0.02	2.16	-
	dynamic A	800	10	1922	138	0.805	4.05 \pm 0.12	4.89	3.80 \pm 0.10
	dynamic B	800	150	34065	2431	0.808	0.97 \pm 0.01	1.03	0.99 \pm 0.03
2	probe	800	33	7280	23	0.809	1.66 \pm 0.01	1.99	-
	dynamic A	1500	33	2111	23	0.708	2.90 \pm 0.05	3.68	3.12 \pm 0.03
	dynamic B	1500	100	6590	73	0.705	1.64 \pm 0.01	1.84	1.79 \pm 0.02
3	probe	800	33	6915	3190	0.792	3.33 \pm 0.10	3.56	-
	dynamic A	2050	33	1164	23	0.854	4.81 \pm 0.11	4.83	4.71 \pm 0.27

TABLE II

RESULTS FROM EXPERIMENTAL MEASUREMENTS THAT USE THE CRB MODEL TO PREDICT PRECISION. FOR EACH PROBE MEASUREMENT THE PRECISION IS ESTIMATED FROM SINGLE HISTOGRAMS USING THE CRB MODEL (EST. δ). N , b AND σ/a ARE THE AVERAGE MEASUREMENTS FOR THE VALUES DESCRIBED IN THE TEXT. THE MEASURED PRECISION (MEAS. δ) IS THE STANDARD DEVIATION OF THE HISTOGRAM LOCALIZATION WHILE THE PREDICTED PRECISION (PRED. δ) IS THE AVERAGE OF THE PREDICTIONS MADE FROM EACH OF THE PROBE HISTOGRAMS WITH N AND b SCALED AS DESCRIBED IN THE TEXT. BOTH EST. δ AND PRED. δ HAVE A ONE STANDARD DEVIATION ERROR RANGE INDICATED.

precision. Future work may incorporate precision estimation into the embedded system of a dToF sensor used for battery-powered applications such as smart canes for visually-impaired people [34]. As the sensor moves and object distances change, the models can predict the current precision and find an optimal exposure time that meets the required precision and no better. This tuning may reduce the power consumption of the system.

Factors related to the sensor optical system, photon propagation, and object scattering are not explicitly included in our models. These factors have well-known relationships to our model parameters: the received signal photons (N), the background photons (b), and the instrument timing spread (σ). This approach of using generalized terms ensures that the models are widely applicable. One could determine a specific factor's effect through the relationship of the factor to N , b , and σ . For example, consider the SPAD photon detection efficiency (PDE) which ranges from 0 to 1. The PDE scales both the signal photons and background photons detected. By referring to (4) we find $\frac{\delta(PDE)}{\delta(PDE=1)} = \sqrt{\frac{1}{PDE}}$. Another factor, object reflectivity (ρ), directly impacts the signal photons collected as $N \propto \rho$, while object reflectivity does not modify the background nor the timing spread. A third important parameter, object distance (r) causes the signal photons to fall off as $N \propto 1/r^2$. Object distance may impact the timing spread depending on the object field-of-view and atmospheric propagation. Two relevant pulsed laser parameters could be evaluated using our models. The laser intensity is directly proportional to the signal photons and the laser pulse-width is one contributor to the total system timing spread. Integration of the detector precision modeling of this work with physics-based optical modeling [27], [28] is a valuable future extension. Other extensions include incorporation of photon pile-up [35], systematic timing errors inherent to merging multiple SPADs or TDCs [36], and linear APD LiDAR systems [37], [38]. This work provides dToF designers and users an accessible yet accurate tool to optimize measurement performance, including in scenarios with power constraints.

ACKNOWLEDGMENT

This work was supported by the University of St. Thomas School of Engineering. We thank undergraduate students Ryan Jans and Jacob Komarek for ToF experimental and analytical support, respectively and Sarah A. Munro for useful discussions.

REFERENCES

- [1] M. Perenzoni, D. Perenzoni, and D. Stoppa, "A 64 \times 64-pixels digital silicon photomultiplier direct TOF sensor with 100-M photons/s/pixel background rejection and imaging/altimeter mode with 0.14km for spacecraft navigation and landing," *IEEE Journal of Solid-State Circuits*, vol. 52, no. 1, pp. 151–160, Jan 2017. [Online]. Available: <http://dx.doi.org/10.1109/JSSC.2016.2623635>
- [2] *VL53LIX Datasheet*, 3rd ed., ST, Nov 2018.
- [3] M.-J. Lee, A. R. Ximenes, P. Padmanabhan, T.-J. Wang, K.-C. Huang, Y. Yamashita, D.-N. Yaung, and E. Charbon, "High-performance back-illuminated three-dimensional stacked single-photon avalanche diode implemented in 45-nm CMOS technology," *IEEE Journal of Selected Topics in Quantum Electronics*, vol. 24, no. 6, pp. 1–9, Nov 2018.
- [4] R. K. Henderson, N. Johnston, S. W. Hutchings, I. Gyongy, T. Al Abbas, N. Dutton, M. Tyler, S. Chan, and J. Leach, "A 256 \times 256 40nm/90nm CMOS 3D-stacked 120 dB dynamic-range reconfigurable time-resolved SPAD imager," in *2019 IEEE International Solid-State Circuits Conference-ISSCC*. IEEE, 2019, pp. 106–108.
- [5] K. Morimoto, A. Ardelean, M.-L. Wu, A. C. Ulku, I. M. Antolovic, C. Bruschini, and E. Charbon, "Megapixel time-gated SPAD image sensor for 2D and 3D imaging applications," *Optica*, vol. 7, no. 4, pp. 346–354, 2020.
- [6] W. Song, J. Lai, Z. Ghassemlooy, Z. Gu, W. Yan, C. Wang, and Z. Li, "The effect of fog on the probability density distribution of the ranging data of imaging laser radar," *AIP Advances*, vol. 8, no. 2, p. 025022, 2018.
- [7] S. Jahromi, J.-P. Jansson, P. Keranen, and J. Kostamovaara, "A 32 x 128 SPAD-257 TDC receiver IC for pulsed TOF solid-state 3-D imaging," *IEEE Journal of Solid-State Circuits*, pp. 1–11, 2020. [Online]. Available: <http://dx.doi.org/10.1109/JSSC.2020.2970704>
- [8] A. Ronchini Ximenes, P. Padmanabhan, M.-J. Lee, Y. Yamashita, D.-N. Yaung, and E. Charbon, "A modular, direct time-of-flight depth sensor in 45/65-nm 3-D-stacked CMOS technology," *IEEE Journal of Solid-State Circuits*, vol. 54, no. 11, pp. 3203–3214, Nov 2019. [Online]. Available: <http://dx.doi.org/10.1109/JSSC.2019.2938412>
- [9] K. Morimoto and E. Charbon, "High fill-factor miniaturized SPAD arrays with a guard-ring-sharing technique," *Optics Express*, vol. 28, no. 9, p. 13068, Apr 2020. [Online]. Available: <http://dx.doi.org/10.1364/OE.389216>
- [10] N. A. W. Dutton, T. Al Abbas, F. M. D. Rocca, N. Finlayson, B. Rae, and R. K. Henderson, "Time of flight imaging and sensing for mobile applications," *Low-Power Analog Techniques, Sensors for Mobile Devices, and Energy Efficient Amplifiers*, pp. 221–249, 2019.
- [11] C. Zhang, S. Lindner, I. M. Antolovic, J. Mata Pavia, M. Wolf, and E. Charbon, "A 30-frames/s, 252 \times 144 SPAD flash LiDAR with 1728 dual-clock 48.8-ps TDCs, and pixel-wise integrated histogramming," *IEEE Journal of Solid-State Circuits*, vol. 54, no. 4, pp. 1137–1151, Apr 2019. [Online]. Available: <http://dx.doi.org/10.1109/JSSC.2018.2883720>
- [12] E. W. Dennison and R. H. Stanton, "Ultra-precise star tracking using charge coupled devices (CCDs)," in *Smart Sensors II*, D. F. Barbe, Ed. SPIE, Jan 1980. [Online]. Available: <https://doi.org/10.1117%2F12.959483>
- [13] A. Small and S. Stahlheber, "Fluorophore localization algorithms for super-resolution microscopy," *Nature Methods*, vol. 11, no. 3, pp. 267–279, Feb 2014. [Online]. Available: <http://dx.doi.org/10.1038/NMETH.2844>

- [14] A. Wallace, R. Sung, G. Buller, R. Harkins, R. Warburton, and R. Lamb, "Detecting and characterizing returns in a pulsed lidar system," *IEEE Proceedings-Vision, Image and Signal Processing*, vol. 153, no. 2, pp. 160–172, 2006.
- [15] A. M. Wallace, J. Ye, N. J. Krichel, A. McCarthy, R. J. Collins, and G. S. Buller, "Full waveform analysis for long-range 3D imaging laser radar," *EURASIP Journal on Advances in Signal Processing*, vol. 2010, pp. 1–12, 2010.
- [16] Xing, Wang, Xu, Lin, Li, Jiao, Zhang, and Liu, "A depth-adaptive waveform decomposition method for airborne LiDAR bathymetry," *Sensors*, vol. 19, no. 23, p. 5065, Nov 2019. [Online]. Available: <http://dx.doi.org/10.3390/s19235065>
- [17] N. Bobroff, "Position measurement with a resolution and noise-limited instrument," *Review of Scientific Instruments*, vol. 57, no. 6, pp. 1152–1157, Jun 1986. [Online]. Available: <https://doi.org/10.1063/2F1.1138619>
- [18] K. A. Winick, "Cramér–Rao lower bounds on the performance of charge-coupled-device optical position estimators," *JOSA A*, vol. 3, no. 11, pp. 1809–1815, 1986.
- [19] R. E. Thompson, D. R. Larson, and W. W. Webb, "Precise nanometer localization analysis for individual fluorescent probes," *Biophysical Journal*, vol. 82, no. 5, pp. 2775–2783, May 2002. [Online]. Available: [http://dx.doi.org/10.1016/S0006-3495\(02\)75618-X](http://dx.doi.org/10.1016/S0006-3495(02)75618-X)
- [20] Y. Shechtman, S. J. Sahl, A. S. Backer, and W. Moerner, "Optimal point spread function design for 3D imaging," *Physical review letters*, vol. 113, no. 13, p. 133902, 2014.
- [21] H. Babcock, Y. M. Sigal, and X. Zhuang, "A high-density 3D localization algorithm for stochastic optical reconstruction microscopy," *Optical Nanoscopy*, vol. 1, no. 1, p. 6, 2012.
- [22] A. J. Berglund, M. D. McMahon, J. J. McClelland, and J. A. Liddle, "Fast, bias-free algorithm for tracking single particles with variable size and shape," *Optics express*, vol. 16, no. 18, pp. 14064–14075, 2008.
- [23] R. J. Ober, S. Ram, and E. S. Ward, "Localization accuracy in single-molecule microscopy," *Biophysical journal*, vol. 86, no. 2, pp. 1185–1200, 2004.
- [24] S. Hernandez-Marin, A. M. Wallace, and G. J. Gibson, "Bayesian analysis of lidar signals with multiple returns," *IEEE Transactions on Pattern Analysis and Machine Intelligence*, vol. 29, no. 12, pp. 2170–2180, 2007.
- [25] G. Chen, C. Wiede, and R. Kokozinski, "Data Processing Approaches on SPAD-Based d-TOF LiDAR Systems: A Review," *IEEE Sensors Journal*, vol. 21, no. 5, pp. 5656–5667, Mar. 2021, conference Name: IEEE Sensors Journal.
- [26] D. Bronzi, F. Villa, S. Bellisai, B. Markovic, S. Tisa, A. Tosi, F. Zappa, S. Weyers, D. Durini, W. Brockherde *et al.*, "Low-noise and large-area CMOS SPADs with timing response free from slow tails," in *2012 Proceedings of the European solid-state device research conference (ESSDERC)*. IEEE, 2012, pp. 230–233.
- [27] P. Padmanabhan, C. Zhang, and E. Charbon, "Modeling and analysis of a direct time-of-flight sensor architecture for LiDAR applications," *Sensors*, vol. 19, no. 24, p. 5464, Dec 2019. [Online]. Available: <https://doi.org/10.3390/s19245464>
- [28] M. Beer, J. Haase, J. Ruskowski, and R. Kokozinski, "Background light rejection in SPAD-based LiDAR sensors by adaptive photon coincidence detection," *Sensors*, vol. 18, no. 12, p. 4338, Dec 2018. [Online]. Available: <https://doi.org/10.3390/s18124338>
- [29] J. D. Valentine and A. Rana, "Centroid and full-width at half maximum uncertainties of histogrammed data with an underlying gaussian distribution-the moments method," *IEEE Transactions on Nuclear Science*, vol. 43, no. 5, pp. 2501–2508, 1996.
- [30] C. R. Rao, "Information and the accuracy attainable in the estimation of statistical parameters," in *Breakthroughs in statistics*. Springer, 1992, pp. 235–247.
- [31] L. J. Koerner. dToF sensor noise simulations and analysis. [Online]. Available: <https://github.com/lucask07/dtof-sim>
- [32] R. M. Jans, A. S. Green, and L. J. Koerner, "Characterization of a miniaturized IR depth sensor with a programmable region-of-interest that enables hazard mapping applications," *IEEE Sensors Journal*, vol. 20, no. 10, pp. 5213–5220, May 2020.
- [33] L. J. Koerner, "Instrbuilder: A Python package for electrical instrument control," *Journal of Open Source Software*, vol. 4, no. 36, p. 1172, 2019.
- [34] W. Elmannai and K. Elleithy, "Sensor-based assistive devices for visually-impaired people: Current status, challenges, and future directions," *Sensors*, vol. 17, no. 3, p. 565, Mar 2017. [Online]. Available: <http://dx.doi.org/10.3390/s17030565>
- [35] A. Gupta, A. Ingle, and M. Gupta, "Asynchronous single-photon 3D imaging," in *Proc. ICCV*, October 2019.
- [36] J. Holma, I. Nissinen, J. Nissinen, and J. Kostamovaara, "Characterization of the timing homogeneity in a CMOS SPAD array designed for time-gated Raman spectroscopy," *IEEE Transactions on Instrumentation and Measurement*, vol. 66, no. 7, pp. 1837–1844, Jul 2017.
- [37] K. Pasquinelli, R. Lussana, S. Tisa, F. Villa, and F. Zappa, "Single-photon detectors modeling and selection criteria for high-background LiDAR," *IEEE Sensors Journal*, vol. 20, no. 13, pp. 7021–7032, Jul 2020.
- [38] D. Li, M. Liu, R. Ma, and Z. Zhu, "An 8-ch LIDAR receiver based on TDC with multi-interval detection and real-time in-situ calibration," *IEEE Transactions on Instrumentation and Measurement*, vol. 69, no. 7, pp. 5081–5090, Jul 2020.

Lucas J. Koerner received B.A. degrees in Integrated Science (Hons), Physics, and Mathematics from Northwestern University in Chicago, IL, USA. He then received the degree of Ph.D. in Physics from Cornell University in Ithaca, NY, USA in 2010. Since 2018 he is an Assistant Professor of Electrical and Computer Engineering at the University of St. Thomas, St. Paul, MN, USA. His research interests include electrical instrumentation development, software for reproducible research, and image sensors.